research papers

Advanced phase-contrast imaging using a grating interferometer

**Samuel Alan McDonald,[a,b] Federica Marone,[a] Christoph Hintermüller,[a]
Gordan Mikuljan,[a] Christian David,[c] Franz Pfeiffer[a,d]‡ and Marco Stampanoni[a,e]***

[a]Swiss Light Source, Paul Scherrer Institut, 5232 Villigen PSI, Switzerland, [b]Department of
Radiology, University of Lausanne Medical School, Lausanne, Switzerland, [c]Laboratory for Micro
and Nanotechnology, Paul Scherrer Institut, 5232 Villigen PSI, Switzerland, [d]École Polytechnique
Federale de Lausanne, 1015 Lausanne, Switzerland, and [e]Institute for Biomedical Engineering,
University and ETH Zurich, 8092 Zurich, Switzerland. E-mail: marco.stampanoni@psi.ch

Phase-sensitive X-ray imaging methods can provide substantially increased
contrast over conventional absorption-based imaging, and therefore new and
otherwise inaccessible information. Differential phase-contrast (DPC) imaging,
which uses a grating interferometer and a phase-stepping technique, has been
integrated into TOMCAT, a beamline dedicated to tomographic microscopy and
coherent radiology experiments at the Swiss Light Source. Developments have
been made focusing on the fast acquisition and post-processing of data to enable
a high-throughput of samples, with obvious advantages, also through increasing
the efficiency of the detecting system, of helping to reduce radiation dose
imparted to the sample. A novel aquarium design allows a vertical rotation axis
below the sample with measurements performed in aqueous environment.
Optimization of the data acquisition procedure enables a full phase volume
(1024 × 1024 pixels × 1000 projections × 9 phase steps, *i.e.* 9000 projections in
total) to be acquired in 20 min (with a pixel size of 7.4 μm), and the subsequent
post-processing has been integrated into the beamline pipeline for sinogram
generation. Local DPC tomography allows one to focus with higher
magnification on a particular region of interest of a sample without the
presence of local tomography reconstruction artifacts. Furthermore, 'widefield'
imaging is shown for DPC scans for the first time, enabling the field of view of
the imaging system to be doubled for samples that are larger than the
magnification allows. A case study is illustrated focusing on the visualization of
soft tissue features, and particularly the substantia nigra of a rat brain. Darkfield
images, based on local X-ray scattering, can also be extracted from a grating-
based DPC scan: an example of the advantages of darkfield contrast is shown
and the potential of darkfield X-ray tomography is discussed.

**Keywords: differential phase contrast; X-ray imaging; synchrotron microtomography;
grating interferometry; darkfield.**

1. Introduction

The use of conventional absorption-based X-ray micro-
tomography can become limited for small samples showing
only very weak attenuation contrast at high energies.
However, a wide range of samples studied in biology and
materials science can produce significant phase shifts of the
X-ray beam. The interaction cross section of the X-ray phase
shift can be as much as three orders of magnitude larger than
that of absorption (Momose & Fukuda, 1995), and thus the
use of the phase signal can provide substantially increased

contrast. An added advantage is that phase signals are
produced with much lower dose deposition than absorption,
which can be very important when radiation damage becomes
an issue. Various phase-sensitive X-ray imaging methods have
been developed, including interferometric methods (Bonse &
Hart, 1965; Momose, 1995, 2003; Bonse & Beckmann, 2001;
David et al., 2002), propagation methods (Snigirev et al., 1995;
Cloetens et al., 1996, 1999; Wilkins et al., 1996), and techniques
using a crystal analyser, such as diffraction enhanced imaging
(Davis et al., 1995; Chapman et al., 1997). These methods differ
significantly in terms of the required experimental set-up and
the physical signal that is measured. The Bonse–Hart crystal
interferometer (Bonse & Hart, 1965) uses a Bragg reflection as

‡ Present address: Department of Physics, Technical University of Munich,
85747 Garching, Germany.

a beam splitter and the recorded signal measures the phase shift $[\Phi(x, y)]$ directly. With the diffraction enhanced imaging or analyzer-based imaging method, the Bragg crystal selects the momentum, local beam deflections are measured and the first spatial derivative of the phase, or phase gradient $(\partial\Phi/\partial y)$, is detected.

For propagation-based phase imaging, the in-line method is often used, where the effects of phase contrast become evident as the sample–detector distance is increased. Propagation turns phase distortions into interference fringes according to Fresnel diffraction. In its simplest form, the measured quantity corresponds to the second derivative of the phase, more complicated expressions arise when larger sample-to-detector distances or strong phase and absorption objects are measured. It is possible to separate the attenuation and phase details from a series of images taken at different distances (Snigirev *et al.*, 1995; Cloetens *et al.*, 1996, 1999; Wilkins *et al.*, 1996). Such a method for the quantitative volumetric reconstruction of the refractive index, as for most methods used for phase tomography, is based on a two-step approach. First, the projections of the phase are determined in the form of Radon projections (phase retrieval), and then the object function, *i.e.* the refractive index decrement, is reconstructed by applying a conventional filtered backprojection algorithm. As an alternative, Bronnikov suggested an algorithm based on the 'transport of intensity' approach which eliminates the intermediate step of two-dimensional phase retrieval (Bronnikov, 1999, 2002). This approach has been implemented by Groso, Stampanoni *et al.* (2006) and Groso, Abela & Stampanoni (2006), with the addition of an absorption-dependent correction factor to the original algorithm in order to reduce the residual absorption artifact, and is referred to as a 'modified transport of intensity' phase-contrast method. When boundary conditions are satisfied such that projections are collected in the near-field Fresnel region, and with homogeneous weak absorption, a good approximation of the refractive index decrement is obtained from a single tomographic dataset. Furthermore, the experimental set-up is very simple and equivalent to that of conventional absorption measurements. Similar arguments have been presented by Gureyev, Nesterets *et al.* (2006) and Gureyev, Paganin *et al.* (2006).

Of the many interferometric methods used for recovering phase information, it is the use of gratings as optical elements in hard X-ray phase imaging that can overcome some of the problems that have impaired the wider use of phase contrast in X-ray radiography and tomography. David *et al.* (2002) demonstrated the use of an interferometer based on two silicon transmission phase gratings and a crystal analyser, originally proposing the grating interferometer consisting of a silicon and a gold grating. Momose *et al.* (2003) subsequently demonstrated two-grating Talbot interferometry in the hard X-ray region for the first time using a pair of transmission gratings (phase and analyser) made by forming gold stripes on glass plates. This work has since been extended to include three-dimensional tomographic phase reconstruction using a hard X-ray two-grating interferometer (Weitkamp *et al.*, 2004, 2005; Momose, 2005). The set-up is mechanically robust,

provided external vibrations are avoided, it is easy to align and has low sensitivity to mechanical drift. There are only a few requirements on monochromaticity and spatial coherence, which becomes more stringent as high sensitivity and therefore larger fractional Talbot distances are required, and the instrument is scalable up to large fields of view. This, combined with the fact that it is particularly sensitive to shallow phase gradients, makes it an ideal technique for soft tissue studies in the fields of medical and biological imaging. Here, the propagation-based method, for example, is much less effective since it relies on the Laplacian of the phase as an origin of contrast. Takeda *et al.* (2008) have recently combined grating interferometry with transmission X-ray microscopy, setting up an X-ray Talbot interferometer so that a moiré fringe pattern appeared on the image plane of an X-ray imaging microscope.

The TOMCAT (tomographic microscopy and coherent radiology experiments) beamline (Stampanoni *et al.*, 2006) of the Swiss Light Source at the Paul Scherrer Institut enables fast, non-destructive, high-resolution imaging measurements in three dimensions. A grating-based differential phase-contrast (DPC) imaging facility has been installed at the beamline, with the aim of having a high throughput of samples in terms of fast data acquisition and post-processing. The technique is complementary to the modified transport of intensity phase-contrast method also used at the beamline (Groso, Abela & Stampanoni, 2006). This propagation-based phase-contrast method is particularly suited for small specimens when high resolution (around 1 µm) is required. The DPC method is characterized by a higher sensitivity to low spatial frequencies and by moderate resolution with larger samples. The aim of this article is to illustrate the DPC imaging technique regarding its implementation. Hardware and software advancements are presented, followed by a discussion of the different imaging techniques that can be applied, including region-of-interest and widefield DPC tomography and dark-field imaging. The application of the techniques is illustrated *via* two case studies, one focusing on the visualization of soft-tissue structures in a rat brain, and the other showing the information gained from darkfield images of a polymer composite sample.

2. Grating-based DPC imaging

2.1. Principle

The principle of DPC imaging with a grating interferometer is shown in Fig. 1 (Weitkamp *et al.*, 2005). A silicon phase grating (G_1) divides the incident X-ray beam into essentially the first two diffraction orders, which, through the Talbot effect (Talbot, 1836; Guigay *et al.*, 2004), form a periodic interference pattern in the plane of the gold analyser or absorption grating (G_2). A phase object placed in the incident beam will cause slight refraction and therefore modifications of the original wavefront profile. These variations result in changes of the locally transmitted intensity through the analyser. This detected signal contains quantitative information on the phase gradient of the object.
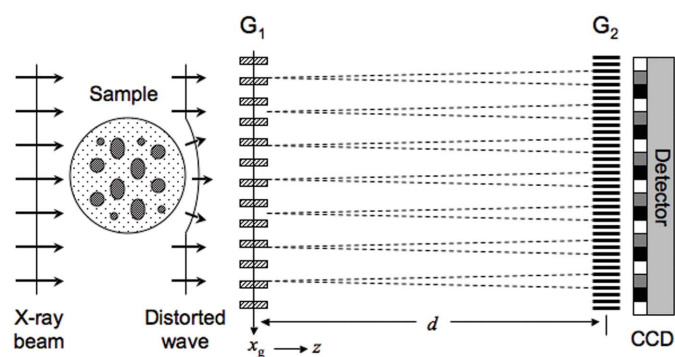
Figure 1
Principle of DPC imaging using a grating interferometer. Through the Talbot effect a periodic interference pattern is formed behind the phase grating (G$_1$) and in the plane of the analyser grating (G$_2$) (Weitkamp *et al.*, 2005).

To separate the phase information from other contributions, a phase-stepping approach is used (Weitkamp *et al.*, 2005). The phase grating is displaced transversely to the incident beam, along x_g, over one grating period whilst acquiring projections for at least four steps for an optimal sinusoidal curve. The intensity signal in each pixel in the detector plane oscillates as a function of x_g. The phase φ of this intensity oscillation in each pixel is related to the wavefront phase profile Φ and to the decrement of the real part of the object's refractive index δ (Born & Wolf, 1980) by

$$\varphi = \frac{\lambda d}{g_2}\frac{\partial \Phi}{\partial x} = \frac{2\pi d}{g_2}\int_{-\infty}^{+\infty}\frac{\partial \delta}{\partial x}\partial z, \quad (1)$$

where g_2 is the pitch of the absorption grating, λ is the X-ray wavelength and d is the distance between the two gratings (Talbot distance).

2.2. Experimental set-up

At the TOMCAT beamline (Stampanoni *et al.*, 2006) at the Swiss Light Source (a medium-energy machine with 2.4 GeV and injection top-up at 400 mA), synchrotron light is delivered by a 2.9 T superbend, with a critical energy of 11.1 keV. This ensures considerable flux at energies >20 keV, thus enabling experiments to be performed with a larger spectrum of hard X-rays. The photon source size (Σ_x, Σ_y) is 124.6 µm horizontally and 37.6 µm vertically (values are given as FWHM). The coherence length l_c is defined as $l_c = \lambda L/s$, where s is the FWHM of an assumed Gaussian source. The coherence length of the beam for the experimental settings used in the case study that follows, namely energy

25 keV ($\lambda = 0.496$ Å) and source-to-sample distance L of 25 m, is 33 µm and 10 µm in the vertical and horizontal directions, respectively (or 16.5 µm × 5 µm, defining the transverse coherence length $l_c = \lambda L/2s$ as the distance to decrease the mutual coherence to a value of 0.5). The size of the X-ray beam at 25 m and energy 25 keV is 15.2 mm horizontally and 3.7 mm vertically. The optics have been kept as simple as possible to prevent degradation of the beam profile and to maintain stability and coherence. A chemical-vapour-deposited 100 µm-thick diamond window (surface roughness 2.5 nm RMS) separates the machine UHV sector (10^{-10} mbar) from the beamline HV (10^{-7} mbar). The main optical component is a fixed-exit double-crystal multilayer mono-chromator, which covers an energy range between 8 and 45 keV. This is located at 7.5 m from the source in order to accept a large angular divergence whilst keeping the optical elements compact. [Ru/C]$_{100}$ and [W/Si]$_{100}$ multilayer stripes have been coated 8 mm apart from each other on a Si $\langle111\rangle$ substrate (active area of 150 mm × 50 mm). As a result, the energy bandwidth of the monochromator is a few percent with multilayer or 10^{-4} when the silicon Bragg reflection is used.

Fig. 2 shows the experimental set-up of the endstation for DPC imaging at the beamline, which consists of two main parts: the hard X-ray grating interferometer and the sample aquarium. The additional hardware required can be quickly and efficiently plugged into the standard endstation set-up, *i.e.* that used for conventional absorption experiments. As shown in Fig. 2, the two gratings are mounted on a support, which is completely decoupled of any contact with the sample stage in
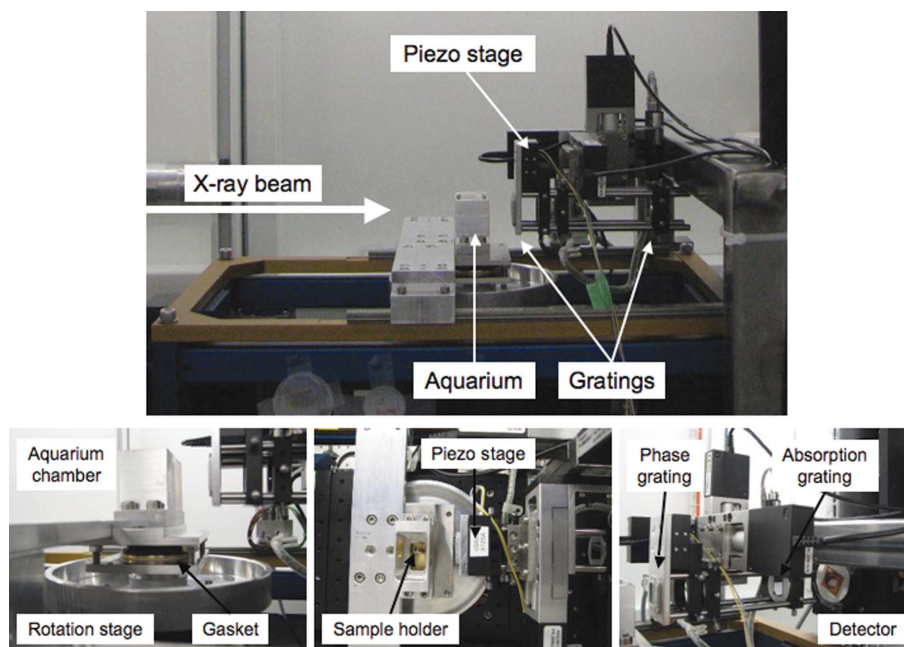

Figure 2
The grating interferometer set-up, with aquarium, for DPC experiments. Top: the interferometer is decoupled from the aquarium/sample-holder to avoid vibration. Bottom left: a novel aquarium gasket design. Bottom middle: the sample holder enters the aquarium bath through a hole at the bottom of the assembly. Bottom right: a high-efficiency high-aperture tandem 1:1 optic detector system is used.

order to avoid vibrations to the gratings during rotation and translation of the sample. The relative distance between the two gratings is adjusted according to the required (fractional) Talbot distance, and while this is done manually they can be moved easily along a track and fixed into position. The grating assembly in its entirety is motorized in three directions corresponding to the orthogonal directions in relation to the X-ray beam. The possibility to remotely displace the assembly in the beam direction is particularly useful for making set-up adjustments. For the phase-stepping approach, the phase grating (G_1) is translated, a movement that has to be accurate, fast and reproducible. This translation is performed with a piezo stage as shown in Fig. 2. The phase grating can be changed according to the required energy, sensitivity and visibility. The difference in the gratings for each of these cases is characterized by a slightly different pitch that takes into account the slightly divergent beam geometry. If this is not considered, stray moiré fringes become visible and the visibility is reduced. Grating G_1 induces a phase shift of π and has a duty cycle of 0.5. The distance between the two gratings for which the interference pattern exhibits a maximum modulation must be a fractional Talbot distance d_m (Weitkamp *et al.*, 2005), given by

$$d_m = m \frac{g_1^2}{8\lambda}. \quad (2)$$

This assumes a plane wave where m is an odd integer corresponding to the order of the fractional Talbot distance, λ is the wavelength of the X-rays and g_1 is the pitch of grating G_1. Note that, taking into account the slightly divergent beam geometry, the distances d_m rescale for a spherical wave (Engelhardt *et al.*, 2007) to

$$d_m^* = \frac{L}{L - d_m} d_m, \quad (3)$$

where L is the distance between the X-ray source and the first grating. The interference pattern shows a lateral period of

$$g_2 = g_1/2, \quad (4)$$

for a plane wave, and

$$g_2^* = \frac{L}{L - d_m} \frac{g_1}{2}, \quad (5)$$

for a spherical wave. Table 1 summarizes the fractional Talbot distances and phase grating pitch for a source-to-sample distance of 25 m. The vertical orientation of the grating lines makes the set-up insensitive to angular fluctuations of the vertically deflecting multilayer monochromator, but, on the other hand, has the disadvantage that the coherence of the beam is not exploited to its fullest.

The capability to scan samples within an aqueous environment is particularly suitable when making phase-contrast measurements of biological samples consisting of soft tissue that need to be kept under conditions that are as close as possible to the native state. For most experiments it is also necessary to measure in a liquid environment to reduce phase wrapping effects. Large phase shifts, such as between tissue

Table 1
(Fractional) Talbot distances and phase grating pitch (g_1) for the first, third, fifth and seventh Talbot orders at energies of 14 keV, 17.5 keV and 25 keV.

Energy (keV)	Talbot order	Talbot distance (mm)	g_1 (µm)
14	1	22.563	3.996
	3	67.566	3.989
	5	112.403	3.982
	7	157.072	3.975
17.5	1	28.197	3.995
	3	84.399	3.986
	5	140.341	3.977
	7	196.019	3.968
25	1	40.262	3.994
	3	120.392	3.981
	5	199.986	3.968
	7	279.035	3.955

and surrounding air at the sample surface for example, manifest themselves in the differential images as points of saturated intensity values (phase wrapping), thus impairing a reliable reconstruction. Such artifacts are reduced in two ways: (i) by performing phase unwrapping during data post-processing, and (ii) by performing scans in a liquid environment that more closely matches the phase of the sample. For this purpose a novel aquarium design has been developed in-house consisting of an aluminium bath with entrance and exit Kapton windows to allow the beam to pass through. The sample holder, which has a base plate at its bottom that is fixed onto the rotation stage, enters the bath through a hole at the bottom of the assembly. Samples are fixed to supports either with wax or glue and the supports are mounted on the sample holder *via* a magnetic contact. In order to ensure smooth rotation of the sample and lateral translation for acquisition of reference images and centring, whilst within the aquarium, a gasket system just below the actual bath (which contains the hole for entry of the sample holder) allows movement of the sample holder whilst the bath remains still (it is fixed to the frame of the endstation sample stage). This is important such that the background intensity in the projections (where there is no sample) remains constant throughout the scan, since the Kapton windows always remain in the beam path. To help remove any air bubbles that may be present in the liquid prior to a scan, a small vibrator can be attached to the aquarium bath. The bath can also be closed and put under vacuum to evacuate any air bubbles.

3. Data acquisition and post-processing

3.1. Fast DPC imaging

Fast data acquisition, whether for phase-contrast measurements or conventional absorption, is achieved with continuous rotation of the sample over 180° whilst the projections are simultaneously collected by the camera. An optimized acquisition software exploits particular properties of the detector: 4 GB internal RAM memory and first-in–first-out (FIFO) buffer acquisition mode. The camera records the projections and temporarily stores them in the camera RAM,

while simultaneously sending the stored images to the file server. This approach reduces the scan time to that of only the equivalent total exposure time, provided this is longer than the readout time. In particular for phase-contrast tomographic data collection the projections for a complete tomogram around a rotation of 180° are recorded for a step of the phase grating prior to moving to the next step. This is opposed to the more traditional static approach, where acquisition of projections for all phase steps is made prior to incrementing the rotation angle. Using such a 'fast-DPC' method eliminates the time needed for the constant grating movement between steps and thus reduces the total acquisition time considerably. This new acquisition method does not impair the quality of the results and makes high-throughput phase-contrast studies possible. For large fields of view, a high-efficiency high-aperture tandem 1:1 optic detector system is used, which also contributes to the fast acquisition of data, and incorporates a 500 µm-thick YAG:Ce scintillator and an objective giving a field of view of 15 mm. This gives a pixel size of 7.4 µm in the reconstructed images when in non-binning mode. The exposure time for a projection is dependent on the scan environment, *i.e.* whether performed in air or liquid, and ranges from ~60 ms to ~250 ms, respectively, at 25 keV. Data for a full DPC scan of 1000 projections and nine phase steps can be acquired in ~20 min. The standard detector, based on a diffraction-limited optical system, offers fields of view ranging from 0.75 mm × 0.75 mm up to 12.1 mm × 12.1 mm with a theoretical pixel size of 0.37 µm and 5.92 µm, respectively. The resolution of the DPC method depends on the (fractional) Talbot distance and is limited by the grating pitch (Weitkamp *et al.*, 2005). As a consequence, DPC scans are performed with a field of view down to 3.6 mm × 3.6 mm with a pixel size of 3.5 µm.

3.2. Phase stepping

While data are needed only over one period of the phase grating (G_1) in order to extract the phase gradient, in practice the phase grating is scanned over two periods. Fig. 3(a) shows a plot of the intensity oscillation as a function of the relative grating position for the same single pixel of a projection during a phase-stepping radiography scan over eight periods of the grating. A periodic change in the amplitude of alternate peaks of the oscillation is observed. This is attributed to the fact that the fabrication process of the gold analyser grating can result in a pitch that is not strictly periodic but shows a 'beating'. It is clear, however, that the oscillation taken over two periods is very reproducible. Furthermore, an important measurement of the performance of a DPC instrument is the visibility, V, of the system, calculated as

$$V = \left| \frac{I_{max} - I_{min}}{I_{max} + I_{min}} \right|, \qquad (6)$$

where I_{max} and I_{min} are the maximum and minimum values of the intensity oscillation such as that shown in Fig. 3(a). Fig. 3(b) shows the visibility map for each pixel of a projection, calculated from a phase-stepping scan with an energy of
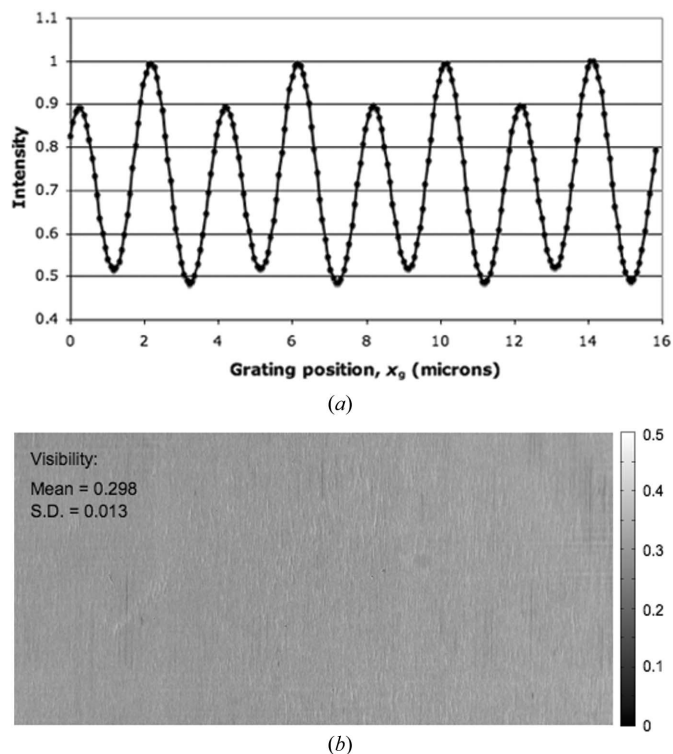

Figure 3
(a) Plot of the intensity oscillation as a function of the grating position x_g for a detector pixel over eight grating periods. The intensity values have been normalized and thus have arbitrary units. (b) Visibility map calculated [using (6)] from the set of projections of the phase-stepping scan. Energy: 25 keV, third (fractional) Talbot distance.

25 keV and the third (fractional) Talbot distance (see Table 1). With such a configuration the visibility is measured to be ~28%. The visibility is limited to this value owing to optical limitations such as the beam coherence, which becomes more important for larger fractional Talbot distances, and grating imperfections. The effect of a finite transverse coherence length l_c on the predicted fringe visibility is given by (Weitkamp *et al.*, 2006)

$$V = \exp\left[-(0.94 m g_2 / l_c)^2\right]. \qquad (7)$$

Inserting the values for m, g_2 and l_c (= 5 µm) into equation (7) results in a predicted visibility of 28%, suggesting that the monochromator does not significantly affect the coherence of the beam. For the third (fractional) Talbot distance and energy 17.5 keV the visibility is measured to be 70%, owing to the fact that the coherence length is a function of the wavelength of the X-rays.

3.3. Local DPC imaging

Local tomographic imaging is of high practical importance where, for example, one wants to obtain data from a small specific region-of-interest (ROI) deep inside a large sample with high resolution. This is performed in a straightforward manner by choosing a fixed reference point, taken as the centre of the sample holder for example, and ensuring that the object rotates about that fixed point. The centring stage on top

of the rotation stage can be adjusted in both the lateral and beam directions by the necessary amounts to translate to the position of the required ROI. Pfeiffer *et al.* (2008*a*) have shown both numerically and experimentally that typical local tomography reconstruction artifacts are absent in DPC tomographic reconstruction. Additionally, continuous rotation of the sample during data acquisition helps to remove such artifacts. When performing local tomography the part of the sample located outside the field of view during rotation covers more than one pixel during the acquisition of one image and therefore contributes with less information to the reconstructed image. Local DPC tomography has been used to focus on a particular ROI within a rat brain sample, illustrated in the case study of §4.

3.4. Widefield DPC imaging

As an alternative to performing a local scan of a particular ROI of a large sample at higher resolution, one might want a small pixel size in the reconstructed images whilst scanning the complete sample. It is possible to double the field of view by collecting projections around a full 360° rotation whilst offsetting the sample and the rotation axis such that the centre of the sample is within the field of view of the detector at all rotation angles. This is a classical approach well known in laboratory computed tomography, often called 'offset (rotate) CT' (Jian *et al.*, 2007). In addition, there must be a position in the projection images at angle k and angle ($k + 180$) where the images overlap such that they can be merged together. Using in-house-developed code the pixel position where the projections overlap is computed automatically and the corresponding merged DPC sinograms are calculated. It is necessary to invert the greyscale of the projection images for angles in the range $k \rightarrow (k + 180)$, where $k = 0$ or 180, so that the phase gradient matches when merging and therefore to avoid a gradient artifact across the reconstructed slice. An example is given in the case study of §4.

3.5. Darkfield imaging

Pfeiffer, Bech *et al.* (2008) have shown how a grating interferometer can also be used to produce X-ray darkfield images. The image contrast is formed through the mechanism of small-angle scattering. Information about the scattering power of an object is contained in the first Fourier component of the intensity oscillation [obtained from a phase stepping scan, Fig. 3(*a*)] in each detector pixel. The amplitude of this component is decreased when X-rays are scattered at internal inhomogeneities as they pass through the object. A projection of an object with darkfield contrast can thus be extracted by calculating the reduction in the amplitude of the intensity oscillations for each pixel. Extraction of the darkfield signal has been implemented into the data post-processing code for generation of corrected projections and the corresponding sinograms. §5 illustrates a short case study carried out on a polymer composite sample for which darkfield imaging has greatly enhanced the detail observed within it, and initial work on darkfield tomographic reconstruction is shown.

3.6. Data post-processing and reconstruction

Post-processing and reconstruction of DPC projection data have been completely integrated into the standard tools developed for conventional absorption tomography. The code developed in-house for the computation of sinograms can handle data acquired from a DPC scan, and can compute corrected projections of the phase gradient from the phase steps at each angle and the corresponding DPC sinograms. Optimization of the code has enabled the availability of a selection of sinograms just a few minutes after the end of the scan such that image quality can be checked and the optimum value of the centre of rotation found. An imaginary filter (Pfeiffer, Bunk, Kottler & David, 2007) has been implemented into the filtered back-projection algorithm so that direct reconstruction of the index of refraction of the object from the DPC sinograms is possible without the need for the extra step of integration of the gradient image to the phase. The complete reconstruction process, from the projection data to the three-dimensional slice data, is performed on a five-node Linux cluster, where each node is equipped with two dual core Xeon processors running at a clock speed of 3.0 GHz (20 CPUs of computing power). Reconstruction of the slices is divided and balanced among the available computing units by DICAT (distributed computing application for tomography), an in-house-developed Java-based client/server application. A $1024 \times 1024 \times 1024$ dataset with 1000 projections and nine phase steps [which corresponds to a total of 18 Gb of raw data, distributed over more than 9000 small (<2.5 Mb) files] can be reconstructed in 10 min.

4. Case study: visualization of the substantia nigra in a rat brain

4.1. Sample preparation

A rat brain was fixed in 4% paraformaldehyde for 2 h before embedding in paraffin such that it was fully dehydrated. To have reconstructed slices free of artifacts and with optimal contrast the samples should not contain air bubbles and a lot of work has been carried out to try to improve and obtain an adequate sample preparation protocol. This work has included altering the length of time the sample is kept in the paraformaldehyde solution prior to paraffin embedding and putting the sample under vacuum during the embedding procedure to try to remove air bubbles.

4.2. Measurement details

The sample was mounted vertically on the flat surface of the sample support such that the brain fitted within the horizontal field of view of the detector system. This vertical sample position also enabled direct reconstruction of coronal slices through the sample; such slices are the most informative when attempting to identify particular regions of the brain. The support with sample was then mounted upon the rotation axis within the aquarium *via* the magnetic contact with the sample holder. The height of the sample as positioned on the support was larger than the vertical height of the beam (field of view).

For this reason a stacked scan routine was used which, when given the top and bottom positions of the sample, calculated the number of blocks (tomographic volumes) required to scan the entire sample. The sample was then automatically translated in the vertical direction such that the bottom line of one block was the top line of the next, until the required number of scan blocks was completed. A total of four blocks were scanned in order to acquire volume data for the whole sample, resulting in a total acquisition time of 84 min. Room-temperature liquid paraffin (chemical formula C_nH_{2n+2} where n = 5–17, density $\simeq$ 0.7 g cm^{-3}) was used as the liquid environment within the aquarium bath in order to achieve the phase matching between sample and surroundings. Use of liquid paraffin also helped to avoid air bubbles owing to its viscosity and poor conductivity. An X-ray energy of 25 keV was selected, using the multilayer $[W/Si]_{100}$ reflection, and a total of 1001 projections (1686 × 501 pixels) were acquired equi-angularly over a sample rotation of 180° for nine phase steps over two periods of the phase grating. Measurements were made using the third (fractional) Talbot distance (see Table 1). The projections were finally post-processed, including flatfield and darkfield corrections, for the extraction of the phase gradient.

4.3. DPC tomographic reconstruction

Overview scans of the full rat brain were performed initially. Fig. 4 shows a sequence of reconstructed coronal slices extracted from various different positions through the three-dimensional tomographic volume of the brain. Fig. 5 shows a three-dimensional representation with a coronal cut through the structure. The images numbered 1–10 in Fig. 4 move from the olfactory bulb region of the brain to the cerebellum, where images 8, 9 and 10 show the white and grey matter. In the case of the rat brain shown in Fig. 4, density differences in the tissue structure are observed at a voxel size of 7.4 µm. In order to perform a quantitative analysis the data were calibrated with respect to the known density of the liquid paraffin. The standard deviation of the grey values in background regions of the reconstructed slices, where there is just liquid paraffin, has been used to give an estimation of the sensitivity of the
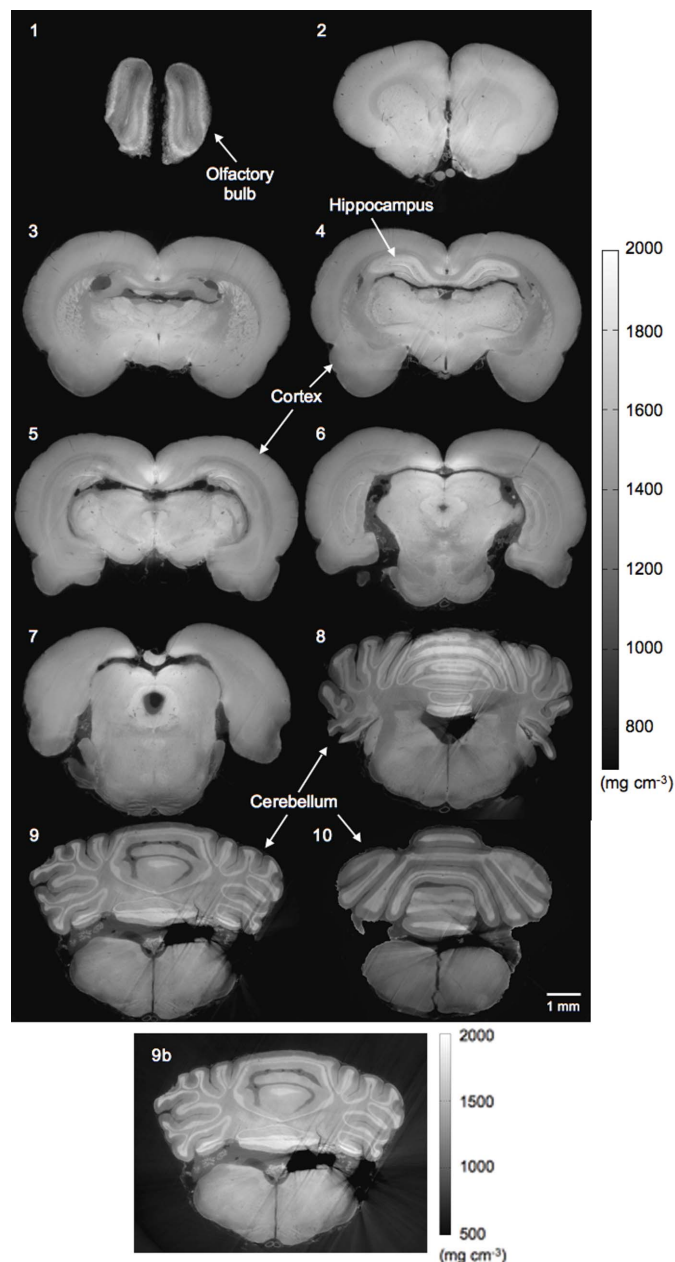

Figure 4
A sequence of coronal slices extracted from different positions through the three-dimensional tomographic volume of the rat brain, reconstructed with a pixel size of 7.4 µm. The reconstructions display quantitatively the mass density according to the colourmap shown. Slice 9b illustrates that of 9 but with an alternative colourmap, with a lower limit of 0.5 g cm^{-3} as opposed to 0.7 g cm^{-3}, in order to reveal the background liquid paraffin together with the air bubbles within the sample.
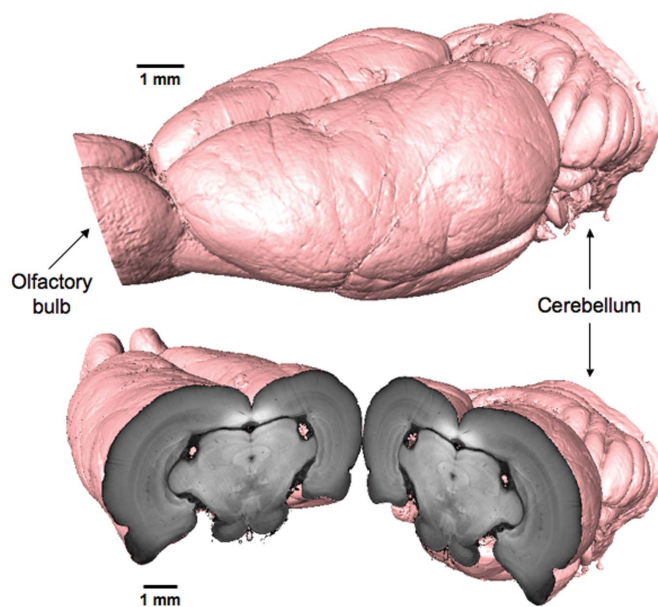

Figure 5
Three-dimensional isosurface of the rat brain, shown both in full and sectioned, illustrating a coronal slice. Note that the images shown in Fig. 4 move from the olfactory bulb region (image 1) to the cerebellum (image 8).

measurement. Based on a mean value for the real part of the index of refraction of the liquid paraffin (C_5H_{12}), δ, of 2.7×10^{-7}, a standard deviation of the background grey values of 4.8×10^{-10} was calculated. This is, far from absorption edges, linearly related to the electron density, ρ, using (Bonse *et al.*, 1997)

$$\delta = \frac{r_0 \rho \lambda^2}{2\pi}, \qquad (8)$$

where r_0 is the electron radius and λ is the X-ray wavelength. This corresponds to a mass density sensitivity of 1.3 mg cm^{-3} for an experimental set-up using the third (fractional) Talbot distance and energy 25 keV. A region equivalent to 1 mm^2 was used to calculate the standard deviation of the background grey values. Note the diagonal lines that appear in the right/bottom part of slice 9. These arise adjacent to bubbles/holes in the sample owing to the large phase shift (phase wrapping effects) between the sample tissue and the air within the bubbles (see slice 9b, Fig. 4). Also, the very bright region that appears in slice 6, with a density of $\sim$2 g cm^{-3}, is thought to be an artifact occurring possibly due to imperfections or non-uniformity in the gratings.

4.4. Conventional absorption tomographic reconstruction

With a grating interferometer one can simultaneously record projections of the conventional transmission signal, which is calculated for each rotation angle by simply averaging the projections from all phase steps. A comparison of equivalent slices reconstructed from the DPC signal and the conventional transmission signal is shown in Fig. 6, illustrating the increased sensitivity of the grating interferometry technique. The latter has been reconstructed using a standard filtered backprojection CT reconstruction method. Note that both images are from the same initial set of projection data and thus result from the same number of projections and exposure time and thus the same X-ray dose imparted to the sample. The advantage of using the DPC signal for detecting
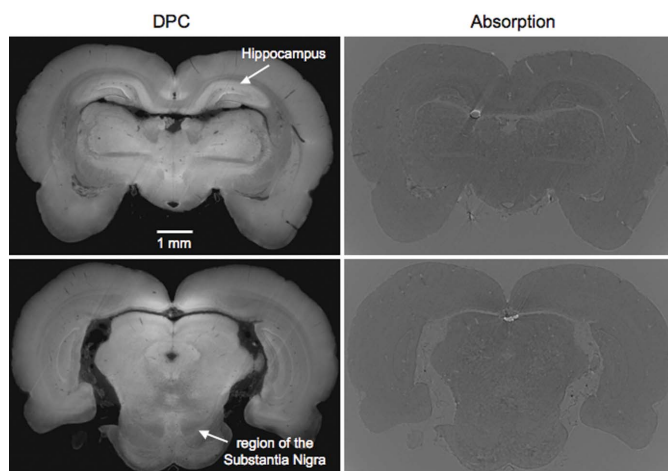

Figure 6
Comparing corresponding reconstructed slices from both the DPC and absorption signals of the rat brain, with the same pixel size of 7.4 μm in both cases.
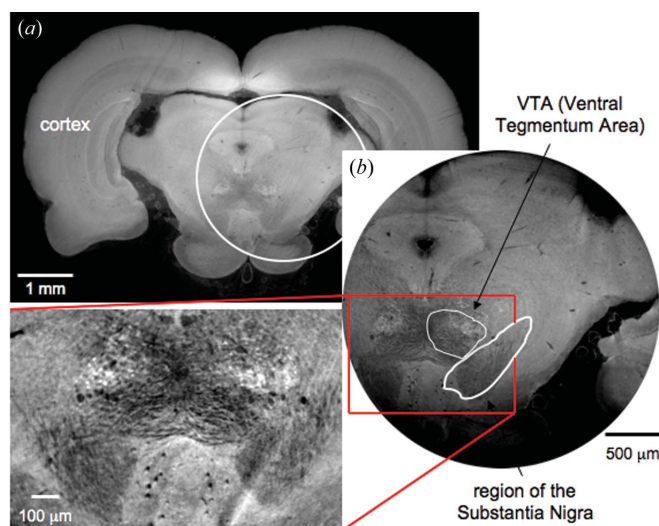

Figure 7
(*a*) Reconstructed overview coronal slice through the three-dimensional tomographic volume of the rat brain at the position of the substantia nigra, and (*b*) slices of the local ROI indicated at a pixel resolution of 3.5 μm.

the tissue structure is clear, for example, when looking at the hippocampus and substantia nigra regions.

4.5. Local DPC reconstruction

Local DPC tomography scans were carried out to focus on a particular ROI at higher resolution. For this the 4× microscope objective was used, giving a field of view of 3.58 mm × 3.58 mm and a reconstructed pixel size of 3.5 μm × 3.5 μm. The local scans were focused around the substantia nigra region of the brain. Fig. 7(*b*) shows a reconstructed slice of a local ROI of the brain corresponding to that indicated in the overview slice (Fig. 7*a*). The darker region of the substantia nigra is observed, together with the nearby ventral tegmentum area, and at such a resolution the blood vessels are also clearly defined.

4.6. Widefield DPC reconstruction

To the authors best knowledge, widefield DPC imaging has been performed for the first time. The rat brain sample was scanned using the 2× microscope objective, having a field of view of 7 mm and thus smaller than the width of the sample (12 mm). Fig. 8 shows a DPC slice through the tomographic volume of the rat brain sample with a pixel resolution of 7 μm, reconstructed from 1441 projections and nine phase steps around a 360° rotation. Image quality is not significantly affected as a consequence of the merging. Note that the inhomogeneity of the reconstructed density value inside the liquid paraffin is thought to be a consequence of imperfections or full-field non-uniformity in the gratings. While scan times are increased by a factor of two over conventional scans (for equivalent sampling frequency), the advantages of the method are clear when complete samples are to be imaged with a small pixel size.
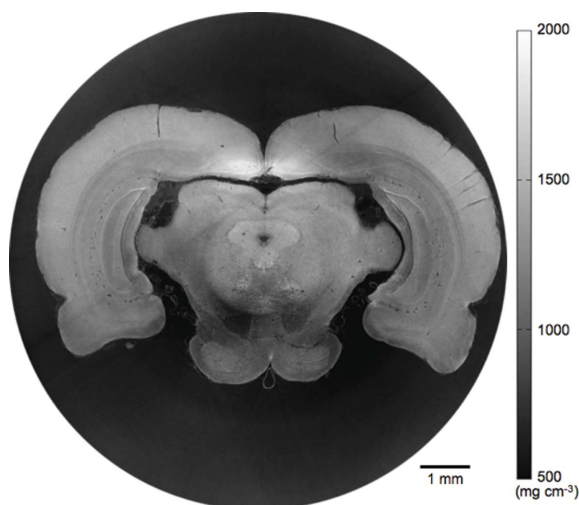
Figure 8
A DPC slice of the rat brain reconstructed with a pixel size of 7 μm. Projections were acquired around a full 360° rotation of the sample and images at angles k and $(k + 180)$ were merged in order to increase the field of view from a width of 7 mm to that encompassing the complete sample (12 mm).

4.7. Summary

The grating-based DPC technique has enabled detailed observation of the soft tissue features within a rat brain, with a pixel size of 7.4 μm × 7.4 μm. Local scans have enabled a particular region of the brain to be focused on, and in particular the region of the substantia nigra, with a pixel size in the reconstructed images of 3.5 μm × 3.5 μm, the theoretical resolution limit of the technique, for the first time. Widefield DPC scans have allowed the field of view of the microscope to be doubled in order to view the complete brain whilst maintaining the high resolution gained from using the higher magnification (smaller field of view) microscope objectives. Pfeiffer, Bunk, David *et al.* (2007) have previously shown the use of the technique for the visualization of a tumor-bearing rat brain, with an effective pixel size in the recorded images of 15.7 μm × 15.7 μm. The sample was fixed and scanned within formalin solution, using a set-up based on the ninth (fractional) Talbot distance to achieve a very high angular and thus phase sensitivity (calculated mass density sensitivity of 0.53 mg cm^{-3}). It should be noted that the investigation of a paraffin-embedded rat brain sample in our study has been performed at the third (fractional) Talbot distance, giving increased visibility, which is limited by the poor coherence in the horizontal direction, whilst achieving adequate sensitivity.

5. Case study: darkfield imaging of a polymer composite

Figs. 9, 10 and 11 illustrate a case study of an object for which the extraction of the darkfield scattering signal has greatly enhanced the contrast. An X-ray energy of 25 keV was used for the experiment, and 1001 projections (1024 × 512 pixels) were acquired over a 180° rotation for nine phase steps over

two periods of the phase grating. Measurements were made using the third (fractional) Talbot distance (see Table 1). The projections were post-processed for extraction of the scattering signal. A conventional absorption projection of a CFRP (carbon fibre reinforced polymer) composite sample is shown in Fig. 9(a). The material has a laminated structure consisting of layers of polymer matrix and carbon fibre reinforcement. The composite sample had been impacted from above such that a depressed region is observed on its surface. Fig. 9(b) shows the corresponding projection of the sample with darkfield contrast. There are clear features in the darkfield image in that three distinct 'regions' have a strong scattering signal. These layers are indeed observed in the absorption image also, albeit with very poor contrast, and seem to contain some fine structure giving rise to such a scattering signal, which is sensitive to fine density variations.

The contrast given by the scattering signal in a projection depends on the angular position of the sample with respect to the X-ray beam. Fig. 10(a) shows a series of projections of the composite sample at different angles and how the signal changes with orientation. This indicates that the orientation of small internal features themselves is important in determining whether or not a darkfield scattering signal is detected.

In order to look at the internal structure being inferred in the darkfield image, data were acquired for a full tomographic scan of the composite sample. Schroer *et al.* (2006) have shown how small-angle X-ray scattering and scanning microtomography can be combined to reconstruct the small-angle diffraction pattern in the direction of the tomographic rotation axis, yielding information about the local nanoscale structure of a sample. Comparing sinograms of the absorption and scattering signals, Fig. 10(b), and the reconstructed slices, Fig. 11, the slice from the scattering signal seems to reveal much more fine detail, that is difficult to discern in the
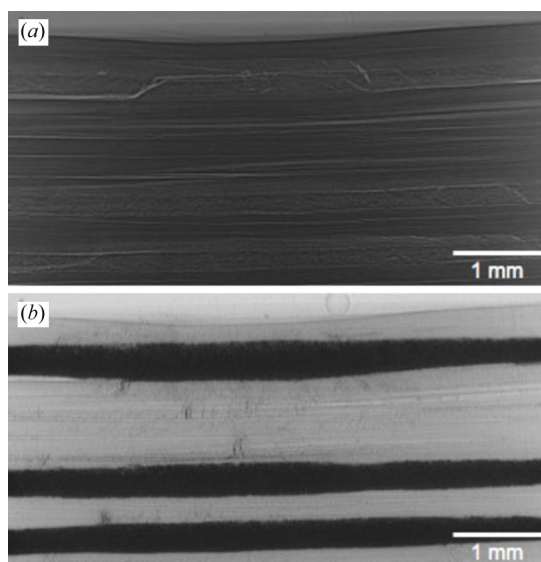

Figure 9
Equivalent projections with extraction of (a) the conventional absorption signal and (b) the darkfield scattering signal, from a phase-stepping scan of a CFRP composite sample.
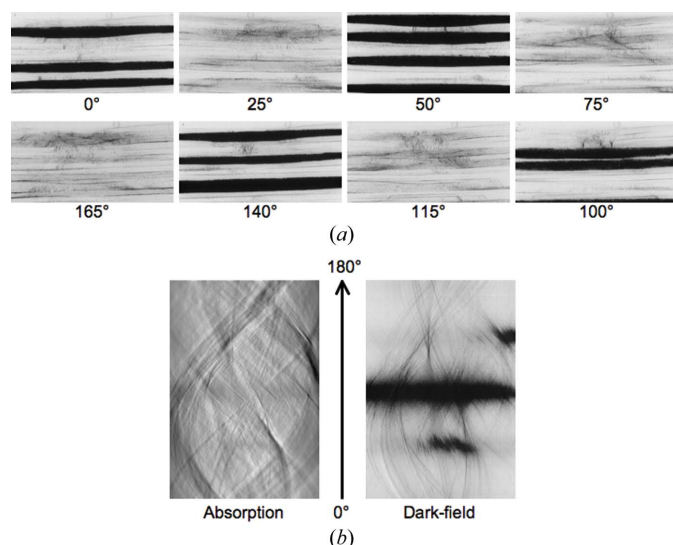
Figure 10
(a) Sequence of darkfield projections of the composite sample at different rotation angles, indicating the dependence of the scattering signal on the angular position of the sample. (b) Comparing absorption and darkfield sinograms.
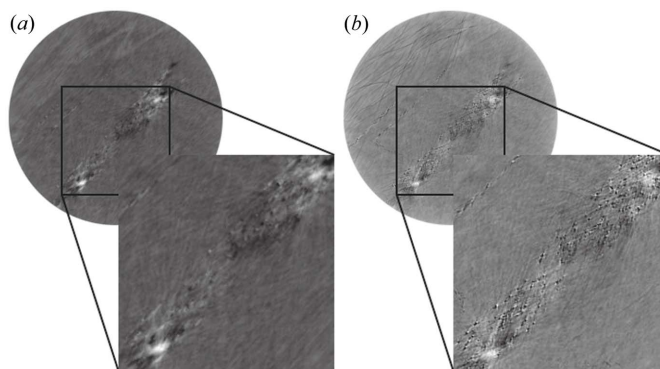

Figure 11
Comparing slices reconstructed from a full tomography scan with extraction of (a) the absorption signal and (b) the scattering (darkfield) signal. It is clear that the darkfield image shows much more detail in terms of the fine structure.

absorption slice. It is important to note that the presented reconstructions are not physically correct in that, as shown in Fig. 10, the set of projections over 180° is not consistent. The pixel intensity given by the scattering signal for a particular 'feature' is only contributed to with a limited number of projections because the signal changes as the object rotates. Further work is necessary to understand the meaning of darkfield sinograms processed from the non-consistent projections, and what the reconstructed slices show in terms of the scattering centres of the fine detail observed.

6. Concluding comments

A grating-based DPC instrument has been fully integrated into the TOMCAT endstation environment, both in terms of fast acquisition and reconstruction. Acquisition and reconstruction of a $1024 \times 1024 \times 1024$ dataset, consisting of 1001 projections and nine phase steps, can be performed in 30 min combined (20 min acquisition, 10 min reconstruction). Effort has also been made to keep it as user-friendly as possible. A range of imaging techniques can be applied, from ROI and widefield DPC tomography to darkfield imaging. The facility opens up the possibility of performing completely new investigations, particularly for soft-tissue studies associated with biological imaging, with a voxel size down to 3–4 μm.

References

Bonse, U. & Beckmann, F. (2001). *J. Synchrotron Rad.* **8**, 1–5.
Bonse, U., Beckmann, F., Bartscher, M., Biermann, T., Busch, F. & Günnewig, O. (1997). *Proc. SPIE*, **3149**, 108–119.
Bonse, U. & Hart, M. (1965). *Appl. Phys. Lett.* **6**, 155–156.
Born, M. & Wolf, E. (1980). *Principles of Optics.* Oxford: Pergamon Press.
Bronnikov, A. V. (1999). *Opt. Commun.* **171**, 239–244.
Bronnikov, A. V. (2002). *J. Opt. Soc. Am. A*, **19**, 472–480.
Chapman, D., Thomlinson, W., Johnston, R. E., Washburn, D., Pisano, E., Gmür, N., Zhong, Z., Menk, R., Arfelli, F. & Sayers, D. (1997). *Phys. Med. Biol.* **42**, 2015–2025.
Cloetens, P., Barrett, R., Baruchel, J., Guigay, J.-P. & Schlenker, M. (1996). *J. Phys. D*, **29**, 133–146.
Cloetens, P., Ludwig, W., Baruchel, J., Dyck, D. V., Landuyt, J. V., Guigay, J. P. & Schlenker, M. (1999). *Appl. Phys. Lett.* **75**, 2912–2914.
David, C., Nöhammer, B., Solak, H. H. & Ziegler, E. (2002). *Appl. Phys. Lett.* **81**, 3287–3289.
Davis, T. J., Gao, D., Gureyev, T. E., Stevenson, A. W. & Wilkins, S. W. (1995). *Nature (London)*, **373**, 595–598.
Engelhardt, M., Baumann, J., Schuster, M., Kottler, C., Pfeiffer, F., Bunk, O. & David, C. (2007). *Appl. Phys. Lett.* **90**, 224101.
Groso, A., Abela, R. & Stampanoni, M. (2006). *Opt. Express*, **14**, 8103–8110.
Groso, A., Stampanoni, M., Abela, R., Schneider, P., Linga, S. & Müller, R. (2006). *Appl. Phys. Lett.* **88**, 214104.
Guigay, J.-P., Zabler, S., Cloetens, P., David, C., Mokso, R. & Schlenker, M. (2004). *J. Synchrotron Rad.* **11**, 476–482.
Gureyev, T. E., Nesterets, Y. L., Paganin, D. M., Pogany, A. & Wilkins, S. W. (2006). *Opt. Commun.* **259**, 569–580.
Gureyev, T. E., Paganin, D. M., Myers, G. R., Nesterets, Y. L. & Wilkins, S. W. (2006). *Appl. Phys. Lett.* **89**, 034102.
Jian, F., Hongnian, L., Bing, L., Lei, Z. & Jingjing, S. (2007). *Nucl. Instrum. Methods Phys. Res. A*, **575**, 519–523.
Momose, A. (1995). *Nucl. Instrum. Methods Phys. Res. A*, **352**, 622–628.
Momose, A. (2003). *Opt. Express*, **11**, 2303–2314.
Momose, A. (2005). *Jpn. J. Appl. Phys.* **44**, 6355–6367.
Momose, A. & Fukuda, J. (1995). *Med. Phys.* **22**, 375–379.
Momose, A., Kawamoto, S., Koyama, I., Hamaishi, Y., Takai, K. & Suzuki, Y. (2003). *Jpn. J. Appl. Phys.* **42**, L866–L868.
Pfeiffer, F., Bech, M., Bunk, O., Kraft, P., Eikenberry, E. F., Brönnimann, C., Grünzweig, C. & David, C. (2008). *Nature Mater.* **7**, 134–137.
Pfeiffer, F., Bunk, O., David, C., Bech, M., Le Duc, G., Bravin, A. & Cloetens, P. (2007). *Phys. Med. Biol.* **52**, 6923–6930.

Pfeiffer, F., Bunk, O., Kottler, C. & David, C. (2007). *Opt. Express*, **15**, 1175–1181.

Pfeiffer, F., David, C., Bunk, O., Donath, T., Bech, M., Le Duc, G., Bravin, A. & Cloetens, P. (2008). *Phys. Rev. Lett.* **101**, 168101.

Schroer, C. G., Kuhlmann, M., Roth, S. V., Gehrke, R., Stribeck, N., Almendarez-Camarillo, A. & Lengeler, B. (2006). *Appl. Phys. Lett.* **88**, 164102.

Snigirev, A., Snigireva, I., Kohn, V., Kuznetsov, S. & Schelokov, I. (1995). *Rev. Sci. Instrum.* **66**, 5486–5492.

Stampanoni, M., Groso, A., Isenegger, A., Mikuljan, G., Chen, Q., Bertrand, A., Henein, S., Betemps, R., Frommherz, U., Böhler, P., Meister, D., Lange, M. & Abela, R. (2006). *Proc. SPIE*, **6318**, 63180M.

Takeda, Y., Yashiro, W., Hattori, T., Takeuchi, A., Suzuki, Y. & Momose, A. (2008). *Appl. Phys. Express*, **1**, 117002.

Talbot, H. F. (1836). *Philos. Mag.* **9**, 401.

Weitkamp, T., David, C., Kottler, C., Bunk, O. & Pfeiffer, F. (2006). *Proc. SPIE*, **6318**, S3180.

Weitkamp, T., Diaz, A., David, C., Pfeiffer, F., Stampanoni, M., Cloetens, P. & Ziegler, E. (2005). *Opt. Express*, **13**, 6296–6304.

Weitkamp, T., Diaz, A., Nöhammer, B., Pfeiffer, F., Rohbeck, T., Cloetens, P., Stampanoni, M. & David, C. (2004). *Proc. SPIE*, **5535**, 137–142.

Wilkins, S. W., Gureyev, T. E., Gao, D., Pogany, A. & Stevenson, A. W. (1996). *Nature (London)*, **384**, 335–337.